# Leading-Edge Vortex Improves Lift in Slow-Flying Bats

F. T. Muijres, *et al.*

*Science* **319**, 1250 (2008);
DOI: 10.1126/science.1153019

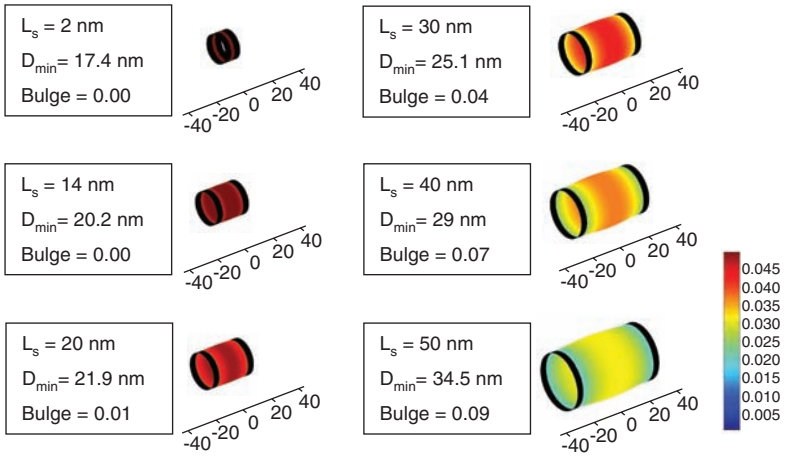


**Fig. 4.** Calculated shapes of membrane tubules constricted by protein rings. The barrel-shaped structures were calculated for different distances $L_s$ between the rings. $D_{min}$ is the minimal diameter at a ring. Bulging between rings is defined as BULGE = $(D_{max} - D_{min})/D_{min}$, with $D_{max}$ being the maximal diameter between rings. The bending rigidity of protein and lipid were assumed to be 800 $k_BT \cdot$ nm and 20 $k_BT$, respectively (where $k_BT$ = 0.6 kcal/mol is the thermal energy). The spontaneous curvature of the protein and the thickness of the protein ring were taken to be 0.13 $nm^{-1}$ and 4 nm, respectively. The color maps represent local mean curvature of the membrane in $nm^{-1}$.

bilayer, a change of the distance between rings from 2 to 50 nm can explain the increase of tubule diameter from 17 nm in the in vitro experiments to ~30 nm in vivo (Fig. 4). The bulging between rings is negligible, even for relatively large distances. Almost perfect cylindrical tubules can thus be generated with the tubule-forming proteins occupying a small fraction of the total membrane surface (fig. S8). We estimate that in fact ~10% of the total tubular ER surface in *S. cerevisiae* could be occupied by the tubule-forming proteins. In reality, the arc-shaped oligomers may be distributed randomly along the tubule, and they may be disassembled actively, which would allow other ER proteins to diffuse in the plane of the membrane.

We hypothesize that the reticulons and Yop1p (DP1) use both their wedgelike shapes and their oligomerization into arcs or rings to generate the tubular ER with minimal surface coverage. Some membrane-shaping proteins, such as synaptotagmin and epsin, use only the wedging mechanism and insert hydrophobic amino acids into the outer leaflet of the bilayer (*13*, *14*), but they need to occupy a large percentage of the membrane surface to induce curvature (*13*). Other proteins, such as the F-BAR proteins and dynamins, primarily form ring- or spiral-shaped scaffolds to generate tubules (*15*–*20*). A combination of the wedging and scaffolding mechanisms, as proposed for the reticulons and Yop1p (DP1), is employed by endophilin and amphiphysin (*9*–*12*, *21*). A combination of the two mechanisms also may be used by other integral membrane proteins that shape organelles. For example, caveolin, which shapes flasklike invaginations of the plasma membrane, called caveoli, has a single hairpin membrane anchor and forms filaments or spirals on the cytoplasmic face of the organelle (*22*). The dynamin-like protein Fzo1p in yeast (Mfn in mammals) in the outer mitochondrial membrane (*23*), which is required for the maintenance of proper mitochondrial tubules, has a hairpin-shaped membrane anchor and oligomerization domains that are essential for its function (*24*, *25*). The proposed mechanisms might thus be generally used to generate organelles with high membrane curvature.

### References and Notes


1. O. Baumann, B. Walz, *Int. Rev. Cytol.* **205**, 149 (2001).
2. G. K. Voeltz, W. A. Prinz, *Nat. Rev. Mol. Cell Biol.* **8**, 258 (2007).
3. S. Bernales, K. L. McDonald, P. Walter, *PLoS Biol.* **4**, e423 (2006).
4. D. W. Fawcett, *The Cell* (Saunders, Philadelphia, ed. 2, 1981).
5. G. K. Voeltz, W. A. Prinz, Y. Shibata, J. M. Rist, T. A. Rapoport, *Cell* **124**, 573 (2006).
6. Materials and methods are available as supporting material on *Science* Online.
7. K. Mitra, I. Ubarretxena-Belandia, T. Taguchi, G. Warren, D. M. Engelman, *Proc. Natl. Acad. Sci. U.S.A.* **101**, 4083 (2004).
8. N. Tolley *et al.*, *Traffic* **9**, 94 (2008).
9. K. Takei, V. I. Slepnev, V. Haucke, P. De Camilli, *Nat. Cell Biol.* **1**, 33 (1999).
10. B. J. Peter *et al.*, *Science* **303**, 495 (2004).
11. M. Masuda *et al.*, *EMBO J.* **25**, 2889 (2006).
12. J. L. Gallop *et al.*, *EMBO J.* **25**, 2898 (2006).
13. S. Martens, M. M. Kozlov, H. T. McMahon, *Science* **316**, 1205 (2007).
14. M. G. Ford *et al.*, *Nature* **419**, 361 (2002).
15. A. Frost, P. De Camilli, V. M. Unger, *Structure* **15**, 751 (2007).
16. W. M. Henne *et al.*, *Structure* **15**, 839 (2007).
17. A. Shimada *et al.*, *Cell* **129**, 761 (2007).
18. K. Takei, P. S. McPherson, S. L. Schmid, P. De Camilli, *Nature* **374**, 186 (1995).
19. J. E. Hinshaw, S. L. Schmid, *Nature* **374**, 190 (1995).
20. B. Marks *et al.*, *Nature* **410**, 231 (2001).
21. J. L. Gallop, P. J. Butler, H. T. McMahon, *Nature* **438**, 675 (2005).
22. K. G. Rothberg *et al.*, *Cell* **68**, 673 (1992).
23. G. J. Praefcke, H. T. McMahon, *Nat. Rev. Mol. Cell Biol.* **5**, 133 (2004).
24. G. J. Hermann *et al.*, *J. Cell Biol.* **143**, 359 (1998).
25. E. E. Griffin, D. C. Chan, *J. Biol. Chem.* **281**, 16599 (2006).
26. Mutations are the result of amino acid substitutions; for example, H7Y indicates that Tyr was substituted for His at position 7. Single-letter abbreviations for the amino acid residues are as follows: A, Ala; C, Cys; D, Asp; E, Glu; F, Phe; G, Gly; H, His; I, Ile; K, Lys; L, Leu; M, Met; N, Asn; P, Pro; Q, Gln; R, Arg; S, Ser; T, Thr; V, Val; W, Trp; and Y, Tyr.


27. We thank D. Moazed, B. Glick, and R. Yan for materials; T. Walz and T. Mitchison for discussions; D. Kelly and G. Skiniotis for comments; and J. F. Ménétret and M. Ericsson for help with EM experiments. C.V. and W.A.P. were supported by the NIDDK intramural program. T.A.R. is a Howard Hughes Medical Institute Investigator.


### Supporting Online Material

www.sciencemag.org/cgi/content/full/319/5867/1247/DC1
Materials and Methods
Figs. S1 to S8
Table S1
References

30 November 2007; accepted 18 January 2008
10.1126/science.1153634

# Leading-Edge Vortex Improves Lift in Slow-Flying Bats

**F. T. Muijres,[1] L. C. Johansson,[1] R. Barfield,[1] M. Wolf,[1] G. R. Spedding,[2] A. Hedenström[1]***

**Staying aloft when hovering and flying slowly is demanding. According to quasi–steady-state aerodynamic theory, slow-flying vertebrates should not be able to generate enough lift to remain aloft. Therefore, unsteady aerodynamic mechanisms to enhance lift production have been proposed. Using digital particle image velocimetry, we showed that a small nectar-feeding bat is able to increase lift by as much as 40% using attached leading-edge vortices (LEVs) during slow forward flight, resulting in a maximum lift coefficient of 4.8. The airflow passing over the LEV reattaches behind the LEV smoothly to the wing, despite the exceptionally large local angles of attack and wing camber. Our results show that the use of unsteady aerodynamic mechanisms in flapping flight is not limited to insects but is also used by larger and heavier animals.**

Generating enough lift during hovering and slow forward flight is problematic according to traditional quasi–steady-state wing theory (*1*, *2*). Yet several species of small flying vertebrates are adapted to foraging using this flight mode. Insects are able to hover by using a range of possible unsteady high-lift mechanisms, including rotational circulation (*3*),

clap-and-fling (*4*, *5*), wake capture (*3*, *6*), and added mass (*7*, *8*). However, arguably the most important mechanism is a leading-edge vortex (LEV) (*5*, *9*–*12*), which may generate up to two-thirds of the total lift in insect flight (*13*, *14*). Although unsteady lift mechanisms have been studied extensively in insects or scaled models of their flapping wings (*5*, *6*, *11*–*17*), vertebrates have only been studied indirectly. Such measurements derived from kinematics or wakes suggest that some birds (*18*) and bats (*19*) require additional lift for weight support, other than quasi–steady-state lift alone (*2*). A recent study of hovering hummingbirds found traces of previously shed LEVs in their wakes (*20*), and sharp-edged model wings of gliding swifts with high sweep (60°) developed stable LEVs (*21*).

We quantitatively measured the airflow, using digital particle image velocimetry (DPIV), around the wings of three individuals of Pallas' long-tongued bat, *Glossophaga soricina* (table S1), flying freely in front of a feeder in a low-turbulence wind tunnel at a forward flight speed $U_\infty = 1$ m/s (*22*). At this flight speed, the average local Reynolds number of the bat wing is $Re \approx 5 \times 10^3$ (*23*) and the Strouhal number $St \approx 1.36$ (*24*).

The DPIV image plane was orientated vertically in the freestream flow direction, and measurements were made at different span-wise locations along the wing, when the wing was positioned horizontally. At this wing position, the wing does not block the DPIV image, the wingspan is at its maximum, and the wing is two-thirds into the downstroke (*22*). Cross-stream DPIV measurements were also performed closely behind the bats (a distance of ~3 mean wing chord lengths at $U_\infty = 1.35$ m/s). From the DPIV data, we determined the two in-plane velocity components of the airflow, resulting in a planar velocity field. Spatial gradients of this planar velocity field also yield the divergence, which is a measure of the variation in out-of-plane velocity (*25*), and the vorticity, which is a measure of the local angular velocity.

From the streamwise DPIV data, the wing profile and its motion (Fig. 1, A to D) were also determined by tracking the part of the wing profile illuminated by the laser sheet (*22*). The velocity of the wing profile was used as a no-slip boundary condition in the DPIV calculations (*22*). The average wing camber is 18 ± 3% (mean ± SD, $n = 68$ observations) of the wing chord (fig. S5D), and the average effective angle of attack is 51° ± 19° ($n = 68$ observations) (fig. S5F) (*22*). Both are high values for steady-state wing theory: A fixed wing at similar *Re* with such high camber and angle of attack would stall and lose lift (*26*).

[1]Department of Theoretical Ecology, Lund University, SE-223 62 Lund, Sweden. [2]Department of Aerospace and Mechanical Engineering, University of Southern California, Los Angeles, CA 90089–1191, USA.

*To whom correspondence should be addressed. E-mail: anders.hedenstrom@teorekol.lu.se

The vorticity field and velocity vectors around the bat wing (Fig. 1) show that the flow separates at the leading edge, generating a patch of high negative vorticity (clockwise spin). But, remarkably, behind this patch of vorticity the airflow reattaches, resulting in attached and laminar flow at the trailing edge. The vorticity patch at the leading edge of the wing was present at all measured span-wise locations but was stronger near the wingtip (Fig. 1C) than toward the wing root (Fig. 1A). Instantaneous streamlines computed from the measured streamwise flow (Fig. 1D) form a recirculating region at the vorticity patch, which also spirals inward at the core. All these facts are consistent with the presence of an attached LEV (*10*). In the neighborhood of the LEV, the divergence of the flow in the image plane is on average positive (source flow) (25) and small compared to the vorticity magnitude (fig. S4). Both sign and magnitude differ from theoretical expectations for LEV stabilization (*10*), which could imply that no LEV stabilizing mechanism is needed (*27*).

In some of the images (mainly distally on the wing), an area of high negative vorticity is also found near the trailing edge but without recirculation (Fig. 1D). The presence of negative vorticity near the trailing edge is associated with the outer wing making a strong rotational (pitch-up) movement before the end of the downstroke (Fig. 1D). Therefore this patch of high vorticity could be a result of rotational circulation (*3*), which is an alternative aerodynamic mechanism for enhanced lift generation.

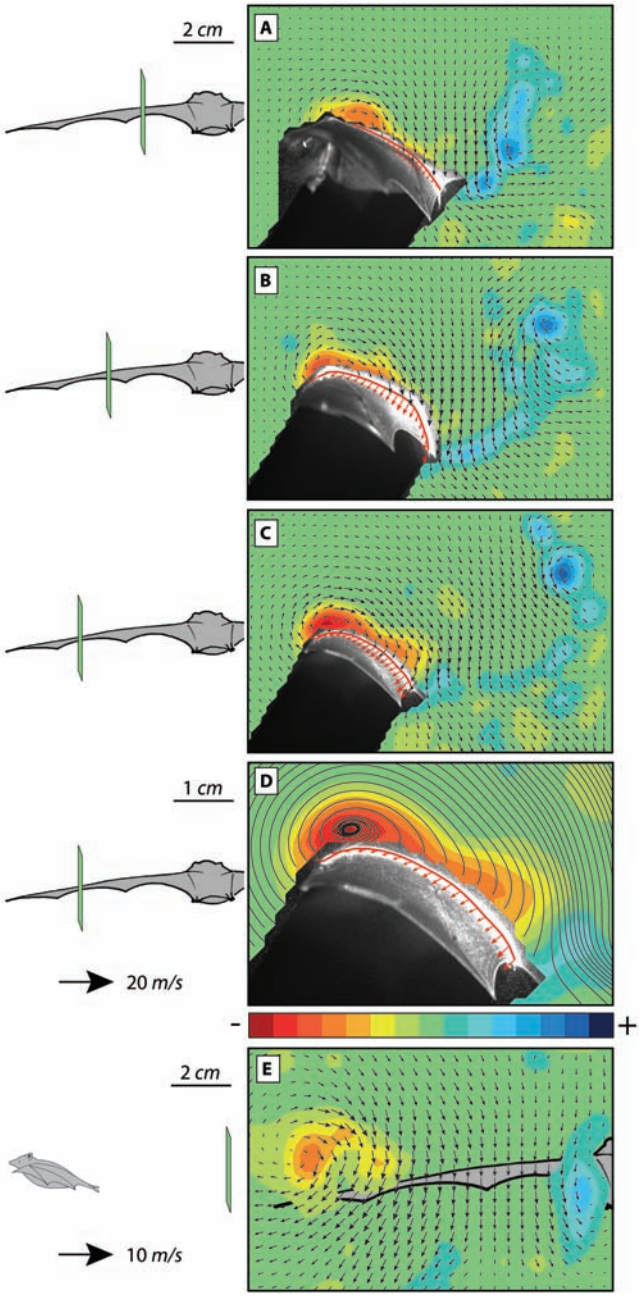


**Fig. 1.** Velocity and vorticity fields around a bat wing in slow forward flight (1 m/s), when the wing is positioned horizontally in the downstroke. The vectors show the disturbance caused by the wing with the uniform mean flow (of 1 m/s) removed. (**A** to **C**) show streamwise measurements at different positions along the span. The span locations are 33, 50, and 65% of the semi-wingspan for (A), (B), and (C), respectively, as indicated on the bat silhouettes to the left. The flight direction is from right to left. Instantaneous two-dimensional streamlines of part of (C) are shown in (**D**). In (A) to (D), The bat wing and its shadow in the DPIV laser sheet are visible; the local wing profile and its relative motion are shown with a red curve and arrows. (**E**) Data derived from cross-stream measurements, with the position of the bat indicated by the bat silhouette. The vorticity field is scaled according to the color bar; it ranges from −1750 to +1750 $s^{-1}$, for (A) to (D) and from −700 to +700 $s^{-1}$ for (E). The velocity vectors are scaled to the reference vector at the left of the color bar for (A) to (D) and at left of (E). Space scale bars are located at left of (A) for (A) to (C), at left of (D), and at left of (E).

To investigate the contribution of the LEV to the total lift, the circulation of the LEV was determined at different span locations (Fig. 2). The average chord length and average effective wing velocity ($\bar{c}$ = 0.042 m and $\bar{U}_{eff}$ = 4.0 m/s) were used to nondimensionalize the circulation ($\Gamma/\bar{U}_{eff}\bar{c}$) (*22*). The results show that the LEV circulation increases toward the wingtip (Fig. 2), which is consistent with LEV structures found for some insects (*1*). When assuming that a LEV enhances lift by adding its own circulation to the bound circulation of a wing (*1*), the nondimensional circulation of the LEV is related to its associated lift coefficient by $C_{LEV} \approx 2 \cdot \Gamma_{LEV}/\bar{U}_{eff}\bar{c}$ (*22*, *28*). The average nondimensional LEV circulation is about 1 (Fig. 3), which corresponds to a $C_{LEV} \approx 2$.

During the downstroke of a flapping wing, positive vorticity is generated at the trailing edge and is shed into the wake. This vorticity can be generated throughout the downstroke, and we will label it trailing-edge vorticity (TEV). According to Kelvin's theorem (*29*), the circulation of the TEV ($\Gamma_{TEV}$) is related to the bound circulation on the wing and thus to the total lift coefficient by $C_L \approx 2 \cdot \Gamma_{TEV}/\bar{U}_{eff}\bar{c}$ (*22*). The shed TEV is clearly visible in Fig. 1, A to C, as a distinct patch of positive vorticity (counterclockwise spin) to the right of the wing, called the start vortex, and a trail of positive vorticity between this start vortex and the trailing edge. Because the tip of the wing travels a larger distance during the downstroke than does the wing root, the start vortex is located further behind the wing near the wingtip (Fig. 1C) than near the wing root (Fig. 1A). This pattern of vorticity shedding is strikingly similar to that of a hawkmoth (*30*). $\Gamma_{TEV}$ was determined at different span locations (Fig. 2), but no systematic variation was found. The average nondimensional $\Gamma_{TEV}$ is 2.4 (Fig. 3), for an effective lift coefficient of 4.8 (*22*), which is beyond that considered to be the maximum possible for quasi–steady-state wings (*2*) at the same *Re* and aspect ratio (*26*), but is similar to results from previous studies of bats (*19*) and within the possible range of pitching and heaving plates (*31*).

As mentioned above, the nondimensional $\Gamma_{LEV} \approx 1$, which means that the LEV contributes to more than 40% of the total lift ($\Gamma_{LEV}/\Gamma_{TEV}$ = 0.42) (*22*). This value is similar to LEV contributions reported for insects [hawkmoth, up to 65% (*13*, *14*), and fruit fly ≈ 45% (*3*)] but is considerably higher than the 15% estimated from the wake of hovering hummingbirds (*20*). The TEV minus the LEV nondimensional circulation is 1.4, resulting in a non-LEV lift coefficient of 2.8 (*22*). This value is also higher than conventional quasi–steady-state wing models at similar conditions (*26*), suggesting that other unsteady lift mechanisms may also be involved, such as rotational circulation (*3*) and delayed stall (*15*), resulting in high lift due to a high angle of attack.

To obtain an image of the three-dimensional wake structure, near-wake cross-stream DPIV measurements were performed for two bats (Fig. 1E). The vorticity field and velocity vectors show the presence of a tip vortex with negative vorticity (clockwise spin) and a weaker vortex near the wing root (root vortex) with positive vorticity (counterclockwise spin). The average tip- and root-vortex circulation were nondimensionalized using the mean wing chord length ($\bar{c}$) and the average effective wing velocity ($\bar{U}_{eff}$) determined from kinematic measurements (*22*). The average tip-vortex circulation has a similar strength as $\Gamma_{TEV}$, and the average $\Gamma_{LEV}$ is 65% of the root-vortex circulation (Fig. 3).

Based on the qualitative and quantitative data, we suggest a cartoon model of the vortex system around the bat wing during the downstroke (Fig. 4). At the beginning of the downstroke, a start vortex is formed at the trailing edge of the wing. During the downstroke, this vortex travels downward and backward because of self-convection, creating a trail of vorticity between the start vortex and the trailing edge of the wing. In inviscid vortex dynamics, a line vortex must terminate either as a closed loop or at a solid surface, and so the start vortex connects to two tip and two root vortices, which grow in length during the downstroke. The tip and root vortices are connected to the wing and to the LEV. The start vortices of each wing are probably connected to each other behind the body (*19*). Because the LEV circulation strength is similar to the root-vortex circulation, these are probably connected, hence the absence of a LEV across the body. The near wake of slow-flying bats did not show a separately shed LEV (*19*), suggesting that the LEV stays attached throughout the downstroke and merges with the stop vortex.

For hovering and slow-flying insects, three different types of LEV systems have been proposed

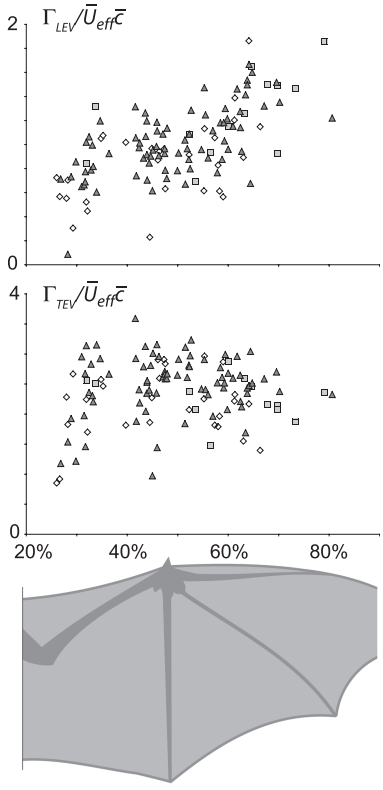


**Fig. 2.** Circulation $\Gamma_{LEV}$ (**top**) and $\Gamma_{TEV}$ (**bottom**) at different wing positions for three bats. The circulation was nondimensionalized using $\bar{c}$ and $\bar{U}_{eff}$ of the measured points (fig. S5). Dimonds represent bat 1, squares represent bat 2, and triangles represent bat 3.

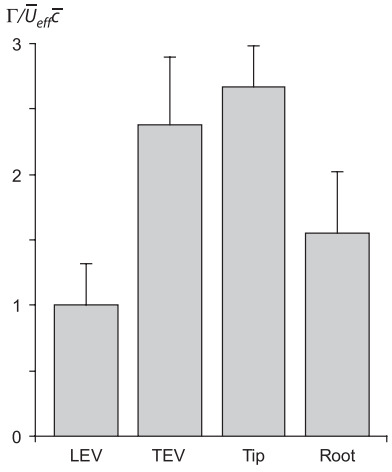


**Fig. 3.** Mean ± SD for circulations in different parts of the wake structure during the downstroke when the wing is horizontal, at a forward speed of 1 m/s. The circulation was nondimensionalized using $\bar{c}$ and $\bar{U}_{eff}$ ( fig. S5). For the LEV and TEV, $n$ = 119 observations; for the tip and root vortex, $n$ = 98 observations (*22*).

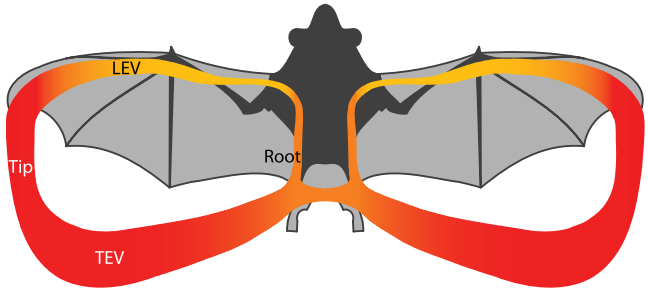


**Fig. 4.** Cartoon of the primary vortex structure for a bat during the downstroke when the wing is horizontal, at a forward speed of 1 m/s. The structure consists of two closed loops, one for each wing, consisting of a LEV on top of the wing, connected to a start vortex shed in the wake via a tip vortex (Tip) and a root vortex (Root). The color coding indicates the absolute value of local circulation; yellow is low circulation and red is high circulation.

(*14*): a helical-shaped LEV starting at the inner wing, increasing in size along the wingspan, and finally connecting to the tip vortex (*9*, *27*); a cylindrical-shaped LEV that expands across the thorax and is connected to the two tip vortices (*6*, *14*); and a LEV that is connected to a small root vortex and a large tip vortex (*5*). The vortex system proposed here (Fig. 4) is most similar to the latter case.

The sharp leading edge of the bat wing probably facilitates the generation of the LEV (*21*), whereas the ability to actively change the wing shape and camber (*32*) could contribute to the control and stability of the LEV.

LEVs have now been observed in active unrestricted bat flight, with a strength that is important to the overall aerodynamics. Unsteady aerodynamic mechanisms for enhanced lift are therefore not unique to insect flight, and larger animals adapted for slow and hovering flight, such as these nectar-feeding bats, can (and perhaps must) use LEVs to enhance flight performance.

**References and Notes**


1. F.-O. Lehmann, *Naturwissenschaften* **91**, 101 (2004).
2. Quasi–steady-state wing theory assumes that the forces on a moving wing are equivalent to the sum of the forces on a fixed wing over a sequence of attitudes that track the wing motion. This model neglects acceleration forces and unsteady aerodynamic effects.
3. M. H. Dickinson, F.-O. Lehmann, S. P. Sane, *Science* **284**, 1954 (1999).
4. T. Weis-Fogh, *J. Exp. Biol.* **59**, 169 (1973).
5. T. Maxworthy, *J. Fluid Mech.* **93**, 47 (1979).
6. R. B. Srygley, A. L. R. Thomas, *Nature* **420**, 660 (2002).
7. C. Ellington, *Philos. Trans. R. Soc. London Ser. B* **305**, 1 (1984).
8. S. Vogel, *Life in Moving Fluids* (Princeton Univ. Press, Princeton, NJ, 1994).
9. C. P. Ellington, C. van den Berg, A. P. Willmott, A. L. R. Thomas, *Nature* **384**, 626 (1996).
10. T. Maxworthy, *J. Fluid Mech.* **587**, 471 (2007).
11. M. W. Luttges, in *Frontiers in Experimental Fluid Mechanics*, M. Gad-El-Hak, Ed. (Springer, Berlin, 1989), pp. 429–456.
12. A. L. R. Thomas, G. K. Taylor, R. B. Srygley, R. L. Nudds, R. J. Bomphrey, *J. Exp. Biol.* **207**, 4299 (2004).
13. C. van den Berg, C. P. Ellington, *Philos. Trans. R. Soc. London Ser. B* **352**, 329 (1997).
14. R. J. Bomphrey, N. J. Lawson, N. J. Harding, G. K. Taylor, A. L. R. Thomas, *J. Exp. Biol.* **208**, 1079 (2005).
15. M. H. Dickinson, K. G. Gotz, *J. Exp. Biol.* **174**, 45 (1993).
16. A. Willmott, C. Ellington, *J. Exp. Biol.* **200**, 2693 (1997).
17. C. Somps, M. Luttges, *Science* **228**, 1326 (1985).
18. U. M. Norberg, in *Swimming and Flying in Nature*, vol. 2, T. Y.-T. Wu, C. J. Brokaw, C. Brennen, Eds. (Plenum, New York, 1975), pp. 869–881.
19. A. Hedenström *et al.*, *Science* **316**, 894 (2007).
20. D. R. Warrick, B. W. Tobalske, D. R. Powers, *Nature* **435**, 1094 (2005).
21. J. J. Videler, E. J. Stamhuis, G. D. E. Povel, *Science* **306**, 1960 (2004).
22. See supporting material on *Science* Online.
23. $Re = \overline{U}_{\mathrm{eff}}\overline{c}/\nu$ ($\overline{U}_{\mathrm{eff}}$ is average effective wing speed, which is the sum of the flight velocity and the wing-flapping velocity; $\overline{c}$ is the average wing chord length; and $\nu$ is the kinematic viscosity of air). *Re* is the ratio between inertial and viscous aerodynamic forces and is an index of the relative instability of the fluid around an airfoil. The bats operate at a *Re* range with rather stable aerodynamic characteristics, just below the *Re* range ($10^4 \leq Re \leq 10^5$) where the aerodynamics are notoriously hard to predict and control.
24. $St = fA/U_{\infty}$ ($f$ is wingbeat frequency and $A$ is the tip-to-tip vertical excursion of the wing tip). *St* is proportional to the ratio of the average wingbeat velocity to the steady forward speed and is an indication of the unsteadiness and efficiency of vortex generation.
25. For an incompressible fluid, the divergence in a planar velocity field is related to the change in out-of-plane flow velocity. When the divergence is positive, the fluid works as a fluid source in the planar velocity field, decreasing the out-of-plane velocity. When it is negative, it is a fluid sink, which increases the out-of-plane velocity.
26. E. V. Laitone, *Exp. Fluids* **23**, 405 (1997).
27. J. M. Birch, M. H. Dickinson, *Nature* **412**, 729 (2001).
28. J. M. Birch, W. B. Dickson, M. H. Dickinson, *J. Exp. Biol.* **207**, 1063 (2004).
29. J. D. Anderson, *Fundamentals of Aerodynamics* (McGraw-Hill, Singapore, 1991).
30. R. Bomphrey, N. Lawson, G. Taylor, A. Thomas, *Exp. Fluids* **40**, 546 (2006).
31. D. A. Read, F. S. Hover, M. S. Triantafyllou, *J. Fluids Struct.* **17**, 163 (2003).
32. S. M. Swartz, M. S. Groves, H. D. Kim, W. R. Walsh, *J. Zool.* **239**, 357 (1996).


33. We thank R. von Busse and Y. Winter for their support. This work was supported by grants from the Swedish Research Council, the Swedish Foundation for International Cooperation in Research and Higher Education, the Knut and Alice Wallenberg Foundation, the Crafoord Foundation, the Magnus Bergvall Foundation, and the Royal Physiographical Society.


**Supporting Online Material**

www.sciencemag.org/cgi/content/full/319/5867/1250/DC1
Materials and Methods
Figs. S1 to S5
Table S1
References and Notes

15 November 2007; accepted 17 January 2008
10.1126/science.1153019

# Synaptic Protein Degradation Underlies Destabilization of Retrieved Fear Memory

**Sue-Hyun Lee, Jun-Hyeok Choi, Nuribalhae Lee, Hye-Ryeon Lee, Jae-Ick Kim, Nam-Kyung Yu, Sun-Lim Choi, Seung-Hee Lee, Hyoung Kim, Bong-Kiun Kaang***

**Reactivated memory undergoes a rebuilding process that depends on de novo protein synthesis. This suggests that retrieval is dynamic and serves to incorporate new information into preexisting memories. However, little is known about whether or not protein degradation is involved in the reorganization of retrieved memory. We found that postsynaptic proteins were degraded in the hippocampus by polyubiquitination after retrieval of contextual fear memory. Moreover, the infusion of proteasome inhibitor into the CA1 region immediately after retrieval prevented anisomycin-induced memory impairment, as well as the extinction of fear memory. This suggests that ubiquitin- and proteasome-dependent protein degradation underlies destabilization processes after fear memory retrieval. It also provides strong evidence for the existence of reorganization processes whereby preexisting memory is disrupted by protein degradation, and updated memory is reconsolidated by protein synthesis.**

Memory retrieval is a process of recalling a previously stored memory. Recently, memory retrieval has attracted much attention because it has been found that inhibition of protein synthesis before or immediately after memory retrieval impairs the previously consolidated memory (*1*–*4*). Retrieval of a consolidated memory thus returns the memory storage site to a labile state, after which new protein synthesis is required for stabilizing or reconsolidating the memory (*1*–*9*). This suggests that the retrieval of the consolidated memory is a dynamic and active process in which remodeling or reorganization of the already-formed memories occurs to incorporate new information (*2*, *3*, *6*).

Although it has attracted less attention than the gene transcription and protein synthesis model for long-lasting synaptic changes and memory stabilization, protein degradation is also critical for long-term memory (*10*–*16*). A major cellular mechanism controlling protein turnover is the ubiquitin and proteasome system, in which polyubiquitinated proteins are degraded by the multisubunit proteasome complex (*11*, *17*). A subunit of the 26*S* proteasome, S5a, which selectively binds to polyubiquitinated proteins, plays a critical role in protein degradation (*18*, *19*).

If retrieval stimuli trigger new protein synthesis for the remodeling of consolidated memory, protein degradation via the ubiquitin and proteasome system might be necessary because remodeling of synapses, which encode the memory, would be mediated by removal of existing proteins and by incorporation of new proteins (*11*). However, little is known about the protein degradation mechanism during the reorganization process after memory retrieval in vivo. We therefore investigated the involvement of the ubiquitin and proteasome system and the roles of protein degradation during the destabilization and restabilization process after fear memory retrieval.

We first performed a total protein polyubiquitination assay after fear memory retrieval

National Creative Research Initiative Center for Memory, Department of Biological Sciences, College of Natural Sciences, Seoul National University, San 56-1 Silim-dong, Gwanak-gu, Seoul 151-747, Korea.

*To whom correspondence should be addressed. E-mail: kaang@snu.ac.kr